Nanoscale

PAPER

View Article Online
View Journal | View Issue

Cite this: *Nanoscale*, 2025, **17**, 22988

Polyoxometalate–cyclodextrin aggregates in isolation: probing the conformer space and binding affinities

Papri Chakraborty, *[a,b] Manuel Link,[c] Christoph Plett, [d] Marco Neumaier, [b] Patrick Weis, [c] Masooma Ibrahim, [b] Stefan Grimme *[d] and Manfred M. Kappes *[b,c]

Non-covalent interactions between polyoxometalates (POMs) and cyclodextrins (CDs) are often utilized to build novel supramolecular architectures for diverse applications. However, structure prediction becomes challenging with the increase in size and complexity of the assemblies. Herein, we investigate the conformer space of isolated non-covalent complexes of a Wells–Dawson type POM $[P_2W_{18}O_{62}]^{6-}$ with cyclodextrins (γ-CD) using trapped ion mobility spectrometry (TIMS). We found that the 1 : 1 (POM : CD) complex exhibits one conformer whereas the 1 : 2 and 1 : 3 (POM : CD) complexes exhibit multiple conformers in the gas-phase, despite showing one stable form in their crystalline phase. The observation of distinct conformers in precise supramolecular aggregates of their complexes reflects the possible isomeric pathways in the growth of the assemblies. The structures of the conformers were resolved through a combination of TIMS and theoretical studies (DFT and GFN1-xTB). Moreover, we performed anion photoelectron spectroscopy (PES) studies, which revealed significant electronic stabilization of the POM anions upon complexation in the γ-CD cavity. This was evident from the increase in adiabatic detachment energy (ADE) of the $[KPOM(\gamma\text{-CD})_1]^{5-}$ complex compared to the $[KPOM]^{5-}$ anion by ~2.4 eV. We also estimated gas-phase binding energies between the POM and γ-CD from the PES studies. Our work provides significant insights into the geometrical and electronic gas-phase structures of POM–CD non-covalent complexes. In the future, this would allow us to precisely design their solid-state assemblies from preformed gas-phase units by mass and isomer-selected ion deposition techniques.

Received 4th July 2025,
Accepted 21st August 2025

DOI: 10.1039/d5nr02831k

rsc.li/nanoscale

1. Introduction

Designing functional hybrid materials often relies on utilizing non-covalent interactions to direct self-assembly into hierarchical structures.[1–4] The motivation to design such supramolecular architectures is to combine or generate new properties in the hybrid material compared to the individual building blocks. Understanding the primary interactions behind the formation of such assemblies is the key to designing better materials with advanced properties. Host–guest chemistry involves complex formation through molecular recognition between two different types of molecules. In this regard, macrocyclic molecules such as cyclodextrins (CDs) are promising to design non-covalent assemblies as their cavity (referred to as α, β, γ, δ, ε, and ξ in the order of increasing diameter) can host various types of molecules such as drugs, peptides, amino acids, *etc.*[5–7] In recent years, a lot of research interest has been devoted into probing interactions of CDs with chemically synthesized inorganic clusters to create functional materials and also metal–organic frameworks with tunable properties.[8–10] Such materials are attractive due to the emergence of new properties such as high porosity and wide applications in drug delivery, gas-storage, chiral separation, sensing, *etc.*[10] Boron clusters such as $B_{12}X_{12}^{2-}$ (X = H, Cl, Br, F) form inclusion complexes with CDs.[11,12] Ligand-protected metal clusters form assemblies with CDs through encapsulation of the organic ligands into the CD-cavity.[8,9,13] Another class of molecules that have gained considerable interest for their potential to form supramolecular complexes with CDs is polyoxometalates (POMs).[14–19]

[a]*Institute for Quantum Materials and Technologies, Karlsruhe Institute of Technology, Kaiserstraße 12, 76131 Karlsruhe, Germany*
[b]*Institute of Nanotechnology, Karlsruhe Institute of Technology, Kaiserstraße 12, 76131 Karlsruhe, Germany. E-mail: manfred.kappes@kit.edu*
[c]*Institute of Physical Chemistry, Karlsruhe Institute of Technology, Kaiserstraße 12, 76131 Karlsruhe, Germany*
[d]*Mulliken Center for Theoretical Chemistry, Universität Bonn, Beringstraße 4, 53115 Bonn, Germany*

POMs are a class of nanosized molecular metal oxide clusters that exhibit wide structural diversity, redox behavior, and magnetic properties and are attractive molecules to incorporate in a hybrid assembly for applications in energy, molecular electronics, and catalysis.[20–24] POMs are discussed as superchaotropic ions[25] and their interaction with CDs results in the formation of ordered hierarchical assemblies. For example, interaction of the archetypal POM $[PMo_{12}O_{40}]^{3-}$ resulted in sandwich complexes where the POM was encapsulated between two CD (β and γ) molecules.[15] POMs with smaller sizes such as $[M_6O_{19}]^{2-}$ (M = Mo, W) were stabilized by deeper inclusion into the cavity of γ-CDs.[26] Molecular recognition between $[P_2W_{18}O_{62}]^{6-}$ and γ-CD was utilized to form 1 : 1, 1 : 2 and 1 : 3 (POM : CD) host–guest complexes.[14] The interactions of Keggin type $[PW_{12}O_{40}]^{3-}$ with α-CD-MOFs were also utilized to form a POM–CD-MOF as a hybrid material.[16] Recently, the effect of the cavity size of CDs on their interactions with the Keggin anion $[PW_{12}O_{40}]^{3-}$ was also probed using CDs of different ring sizes (α, β, γ, δ, ε, and ξ).[19] The superchaotropic effect of POMs and their host–guest interaction with CDs were utilized to create stimuli-responsive polymers.[27] The size and structure of the POM, as well as the cavity size of the CD, are key factors in tuning the nature of the interactions and hence creating a wide variety of self-assembled structures. Moreover, both POMs (depending on their geometrical structure) and CDs offer multiple binding sites that may in principle form a wide range of conformers of these supramolecular adducts. This aspect remains less explored. Also, the interactions and kinetics associated with adduct formation in the crystalline state and solution phase may differ from adduct formation in isolation thus leading to different structures. This would in turn allow the assembly of new solid phases from preformed gas-phase units.

As the size of molecular assemblies increases, predicting their structures in isolation becomes more complex, making it challenging to identify all possible conformations of these large, flexible systems. Understanding these interactions in detail will enable us to design the assemblies with better control over the conformer-selectivity during the growth of the assemblies. While X-ray diffraction (solid-state) and NMR spectroscopy (solution) have been most widely used to study condensed phase structures and interactions, in recent years, ion mobility mass spectrometry (IM MS) (gas-phase) has become powerful to resolve structures for large non-covalent assemblies in isolation.[19,28–32] This technique allows separation of gas-phase conformers of ions due to a difference in their collision cross-sections (CCS). The structures are determined indirectly through comparison of the experimental CCS and the calculated CCS from, *e.g.*, trajectory methods of computed structure candidates. IM MS was earlier used to study structures of POMs in the gas-phase.[33,34] In a recent study, Su *et al.* used IM MS to study the gas-phase structures of 1 : 1 complexes of a Keggin type POM $[PW_{12}O_{40}]^{3-}$ with CDs (α, β, γ, δ, ε, and ζ) and compared the gas-phase structures to that in solution using NMR spectroscopy.[19] However, studies on quantifying the conformational space of higher aggregates of CDs with POMs have not been performed yet.

Herein, we studied the structures of supramolecular aggregates of the Wells–Dawson POM $[P_2W_{18}O_{62}]^{6-}$ with γ-CD by IM MS. While only one conformer was observed for the 1 : 1 POM : γ-CD complex, multiple conformers were observed for the 1 : 2 and 1 : 3 adducts. This reflected isomeric pathways of growth of the assembly resulting from complexation through different binding sites of the POM and γ-CD. In contrast, one stable form of the adducts was previously observed in their crystalline state.[14] DFT calculations were used to determine the gas-phase structure of the adducts which were found to be different compared to their previously characterized condensed-phase structures.[14] We also used the semi-empirical GFN1-xTB[35,36] quantum chemistry method to compute structural models for larger assemblies, *i.e.* 1 : 3 (POM : CD) adducts, and determine their structures by comparison with experimental IM MS data. Moreover, to provide further information on the species probed, we also used anion photoelectron spectroscopy (PES) to estimate the electron binding energies (EBEs) of the POM anion in isolation and in a complexed form with γ-CD. Experimental PES data, together with computational studies on the electronic structures, allowed the confirmation of adduct structure types, suggested electronic stabilization of the POM anion in the cavity of the neutral γ-CD molecule and also enabled us to estimate the gas-phase binding energies (BEs) between the POM and γ-CD. Determination of BEs contributes a significant step towards more quantitative discussion of the superchaotropic effect of POMs.[37] Our work provides molecular level insights (at both the structural and electronic levels) into the host–guest complexation between the POM and γ-CD, in the absence of any solvent or condensed phase interactions.

2. Experimental and computational methods

2.1. Synthesis of the Wells–Dawson POM $K_6[P_2W_{18}O_{62}]\cdot 14H_2O$

$K_6[P_2W_{18}O_{62}]\cdot 14H_2O$ was synthesized following reported methods.[38] $Na_2WO_4\cdot 2H_2O$ (300 g; 0.91 mol) was dissolved in 350 mL of distilled water. This solution was acidified by fractional addition of 4 M HCl (250 mL; 1.00 mol) under vigorous stirring. When the cloudy solution became clear again, 4 M H_3PO_4 (250 mL; 1.00 mol) was added slowly. The pale-yellow solution was refluxed for at least 24 h. After this reaction time, the yellow color of the solution became more intense. This solution was allowed to cool to room temperature and was further treated with 150 g of KCl. The precipitate which appeared was filtered off and air-dried. This crude material was dissolved in 650 mL of distilled water in order to remove any insoluble impurities through filtration. The transparent solution was then heated to roughly 90 °C for at least 48 h in order to make it concentrated. After this period of time, the solution was allowed to cool to room temperature before being placed finally in a refrigerator at 4 °C. After a few days, yellow crystals of $K_6[P_2W_{18}O_{62}]\cdot 14H_2O$ were collected (232.5 g; 95%) (air, water and heat stable).

2.2. Electrospray ionization mass spectrometry (ESI MS) and trapped ion mobility spectrometry (TIMS)

ESI MS and TIMS ion mobility measurements were performed on a Bruker TIMS-TOF mass spectrometer. The mass spectrometer was equipped with an electrospray source and the measurements were performed in the negative ion mode. The following conditions were used for the ESI process: capillary voltage: 3000 V, end plate offset: 2000 V, dry temperature: 200 °C, dry gas: 3.5 l min^{-1} and nebulizer: 0.3 bar.

The TIMS parameters were as follows: IMS tunnel voltages, delta 1: 20 V, delta 2: 20 V, delta 3: −30 V, delta 4: −20 V, delta 5: 0.0 V, delta 6: −20 V, IMS ramp time: 500 ms and inverse mobility gap (ramp end – ramp start): 0.4 V s cm^{-2}. TIMS data were recorded with m/z selection for each of the species. Determination of $^{TIMS}CCS_{N_2}$ requires calibration. For this, the commercially available Agilent tuning mix and the reported drift tube CCS of the calibrant ions were used.[39] The Bruker TIMS TOF platform records the ion intensities as a function of inverse mobilities ($1/K$). To generate the mobilograms (as shown in the results), the recorded values of $1/K$ were converted to $^{TIMS}CCS_{N_2}$ using the Mason–Schamp equation.

2.3. Photoelectron spectroscopy (PES)

PES spectra were taken for the POM and different POM(γ-CD) complexes using a previously reported machine.[40] A new laser system from EKSPLA (NT342 Series, 20 Hz pulse frequency, ns pulses) was introduced to the instrument. It utilizes an OPO to generate wavelengths between 210 nm and 2000 nm. Further experimental details on the PES measurements are included in the SI.

2.4. Computational details

The γ-CD and POM input files were obtained from crystal structures[14] with subsequent GFN1-xTB[36] optimization. Different interaction sites between the γ-CD and the POM molecule were probed with the automated Interaction Site Screening (aISS)[41] algorithm and GFN1-xTB geometry optimizations implemented in the xTB[35] program package version 6.6.0. Additional structures were generated manually by following symmetrical criteria and subsequently optimized with GFN1-xTB. r^{2}SCAN-3c[42] geometry optimizations, Hessian calculations, and ωB97X-V[43] and PBE0-D4 single-point energy calculations were performed using ORCA[44] version 5.0.3. Default settings of the respective program packages were applied if not stated otherwise. Mulliken charges for the CCS calculations were taken from the respective method used for geometry optimizations.

2.5. Trajectory calculations

The calculation of $^{TM}CCS_{N_2}$ was performed with IMoS 1.09 using the trajectory method (TM) in N_2 gas.[45] Atomic coordinates and Mulliken partial charges obtained from DFT (r^{2}SCAN-3c) and GFN1-xTB calculations were used as input parameters. The trajectory calculations were carried out at 300 K and the ion-induced quadrupole potential was considered explicitly.[46] For all structures, we simulated 3×10^7 trajectories (1×10^7 trajectories per rotation of the molecule) to reduce the statistical error (standard error of the mean) to around ±0.3–0.4%. The standard error of the mean for a simulation of 3×10^7 trajectories was determined for different complex types by simulating 10 times 3×10^6 trajectories.

3. Results and discussion

3.1. Synthesis and structure of $[P_2W_{18}O_{62}]^{6-}$

The Wells–Dawson POM, denoted as $[P_2W_{18}O_{62}]^{6-}$, was synthesized according to the reported method[38] (see experimental methods above) and characterized using ESI MS (Fig. S1). The structure of the POM anion is presented in Fig. 1A. Its central region resembles a belt formed by two tetrahedral PO_4 groups, surrounded by an array of 12 equatorial tungsten (W) atoms. These W atoms occupy the centers of WO_6 octahedra arranged in an alternating pattern of corner- and edge-sharing connections. On each side of the belt, three edge-sharing WO_6 octahedra form cap-like arrangements that enclose the top and bottom of the structure. This overall architecture exhibits D_{3h} symmetry and high thermal and chemical stability, making it a valuable model for catalytic and materials applications.

3.2. ESI MS of the POM and POM–γ-CD adducts

During the electrospray process, the POM ionized in multiple charge states in the negative ion mode depending upon the number of counter ions (H^+/K^+) attached to the molecular ion and were primarily observed as $[HPOM]^{5-}$ (m/z 873), $[KPOM]^{5-}$ (m/z 880), $[K_2POM]^{4-}$ (m/z 1110) and $[K_3POM]^{3-}$ (m/z 1493) (Fig. S1). The POM (structure in Fig. 1A) and γ-CD (structure in Fig. 1B) were mixed in a 1 : 3 molar ratio to allow the formation of their complexes in solution (water–acetonitrile mixture) as reported earlier.[14] The concentrations of the POM and γ-CD solutions were 1 mM. The resulting mixture was analyzed by ESI MS and up to three γ-CD attachments to the POM were observed in ESI MS, as shown in Fig. 1C. A series of peaks were observed that corresponded to the species $[POM(\gamma\text{-CD})_1]^{6-}$ (m/z 943), $[POM(\gamma\text{-CD})_2]^{6-}$ (m/z 1159), $[POM(\gamma\text{-CD})_3]^{6-}$ (m/z 1376), $[KPOM(\gamma\text{-CD})_1]^{5-}$ (m/z 1139), $[KPOM(\gamma\text{-CD})_2]^{5-}$ (m/z 1399), $[KPOM(\gamma\text{-CD})_3]^{5-}$ (m/z 1658), $[K_2POM(\gamma\text{-CD})_1]^{4-}$ (m/z 1434), $[K_2POM(\gamma\text{-CD})_2]^{4-}$ (m/z 1759), and $[K_2POM(\gamma\text{-CD})_3]^{4-}$ (m/z 2083). The composition of the observed supramolecular complexes may be generalized as $[K_xPOM(\gamma\text{-CD})_n]^{(6-x)-}$ (x = 0–2, n = 1–3). The assignment of the species was further confirmed from the comparison of the experimental and simulated isotopologue patterns for each of these species (Fig. S2). Note that in a previous report by Moussawi *et al.* also, some of these complexes were observed in ESI MS.[14] However, a larger number of complexes are observed here likely due to different concentrations of the reaction mixture and electrospray conditions, compared to the earlier report.

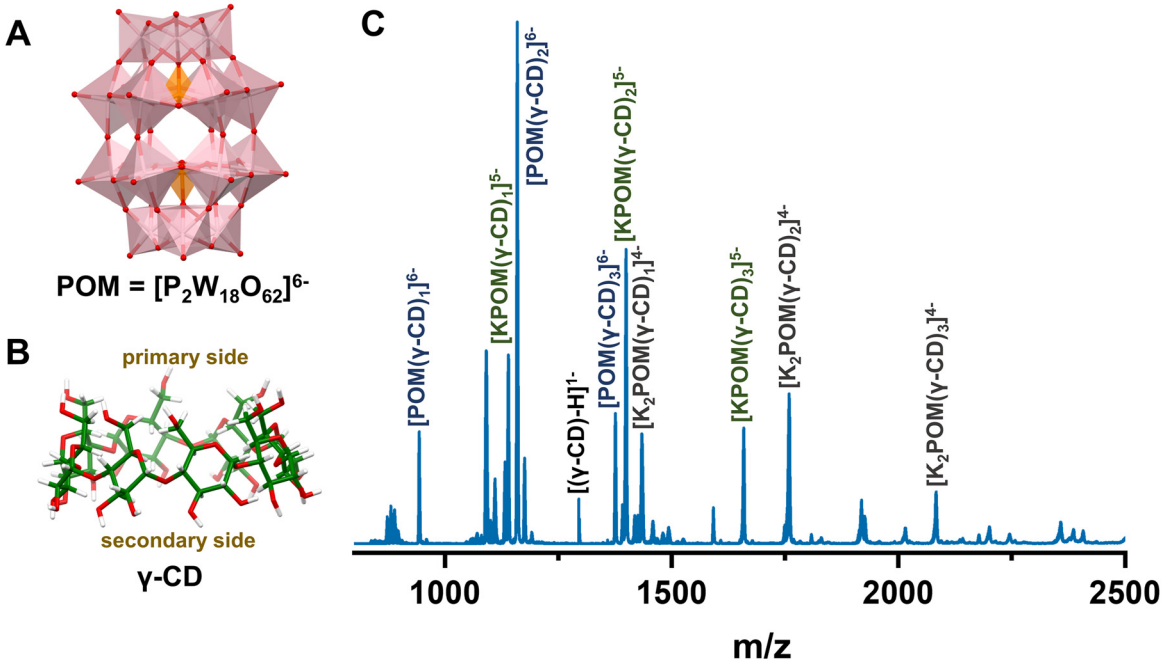

Fig. 1 (A) Structure of $[P_2W_{18}O_{62}]^{6-}$ (POM), (B) structure of γ-CD, (C) ESI MS of the mixture of the POM and γ-CD. Color codes: pink: WO_6 octahedron and W at the centre, red: O, orange: P and PO_4 tetrahedron, green: C and white: H.

3.3. TIMS studies on adducts of the POM with γ-CD, $[POM(\gamma\text{-CD})_n]^{6-}$ (n = 1–3)

To determine the gas-phase topologies, we subjected the desired ions to TIMS[47] measurements that allow determination of their CCS in N_2 gas ($^{TIMS}CCS_{N_2}$). The $^{TIMS}CCS_{N_2}$ values reported here correspond to the mean of measurements taken over three separate days, with the standard error of the mean also provided (see Table S1). First, we performed TIMS studies on the isolated POM in different charge states and a single peak corresponding to one stable form was observed in each of the species, $[HPOM]^{5-}$ ($^{TIMS}CCS_{N_2}$ = 515.4 ± 0.4 Å^2), $[KPOM]^{5-}$ ($^{TIMS}CCS_{N_2}$ = 520.7 ± 0.5 Å^2), $[K_2POM]^{4-}$ ($^{TIMS}CCS_{N_2}$ = 445.9 ± 0.5 Å^2) and $[K_3POM]^{3-}$ ($^{TIMS}CCS_{N_2}$ = 390.0 ± 0.3 Å^2) (Fig. S3). Note that $^{TIMS}CCS_{N_2}$ slightly increases by replacement of H^+ with K^+ in the 5^- charge state of the POM. The significant increase in $^{TIMS}CCS_{N_2}$ with increasing negative charge on the $[K_xPOM(\gamma\text{-CD})_n]^{(6-x)-}$ complex arises from stronger charge-induced dipole interactions with the collision gas N_2. Furthermore, we focused on determining the gas-phase structures of $[POM(\gamma\text{-CD})_n]^{6-}$ (n = 1–3). TIMS measurements on these ions are presented in Fig. 2. The species $[POM(\gamma\text{-CD})_1]^{6-}$ showed one peak with $^{TIMS}CCS_{N_2}$ of 665.0 ± 3.1 Å^2. However, for $[POM(\gamma\text{-CD})_2]^{6-}$, two distinct peaks corresponding to two different isomers were observed with $^{TIMS}CCS_{N_2}$ of 728.6 ± 0.5 Å^2 and 738.4 ± 0.4 Å^2. For the larger adduct with three γ-CDs attached, $[POM(\gamma\text{-CD})_3]^{6-}$, four distinct isomers were observed with $^{TIMS}CCS_{N_2}$ values of 790.6 ± 0.6 Å^2, 798.7 ± 0.6 Å^2, 821.2 ± 0.6 Å^2 and 825.1 ± 0.5 Å^2. The multiple isomers observed in the case of the complexes of the POM with two and three γ-CDs likely arise due to possible interactions at different binding sites of the molecules, while for $[POM(\gamma\text{-CD})_1]^{6-}$, only one isomer seems to be formed. The supramolecular complexes in the gas-phase will be stabilized primarily by the hydrogen bonding (HB) interactions between the terminal surface oxygen atoms of the POM and the –OH groups of the γ-CD. Other non-covalent interactions like ion–dipole and van der Waals interactions will also contribute to the stabilization of the complexes.

3.4. Theoretical studies and discussion of TIMS results

3.4.1. Gas-phase structure of $[POM(\gamma\text{-CD})_1]^{6-}$. The Wells–Dawson POM $[P_2W_{18}O_{62}]^{6-}$ presents both a longitudinal (long axis) belt region and capping surfaces where the γ-CD molecules can interact. Moreover, the γ-CD molecule is flexible in nature and conformational changes can occur by bond rotations at the glycosidic linkages or the hydroxyl groups. Previous ion mobility studies on complexes of γ-CD molecules with metal ions revealed the presence of multiple conformers.[48,49] The various interaction sites of the POM combined with the conformational flexibility of γ-CD potentially lead to a large conformational space, where the conformational stability will be affected by the nature of the interactions of the POM surface and the γ-CD ligand. For $[POM(\gamma\text{-CD})_1]^{6-}$, we observed one stable structure in the gas-phase, suggesting only one stable conformer. This suggests that the conformational flexibility of the γ-CD ring is restricted when bound to the surface of the POM and that there is obviously one single preferred coordination site of γ-CD to the POM. To determine the structure of isolated $[POM(\gamma\text{-CD})_1]^{6-}$, we first carried out quantum chemistry based molecular docking calculations

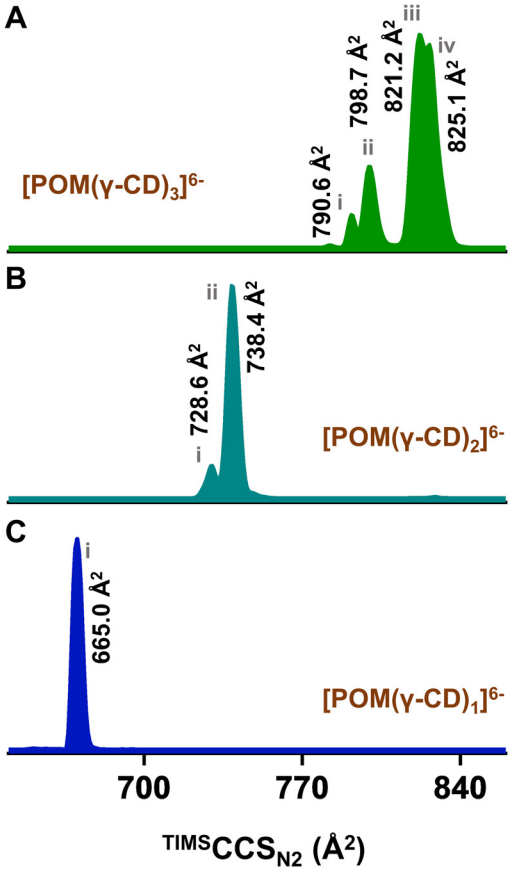

Fig. 2 TIMS spectra of $[POM(\gamma\text{-CD})_n]^{6-}$ (A) n = 3, (B) n = 2 and (C) n = 1. $^{TIMS}CCS_{N_2}$ values denoted here are mean values based on measurements from three different days. The standard error is 3.1 Å^2 for n = 1 and ≤0.6 Å^2 for n = 2, 3. (POM = $P_2W_{18}O_{62}$).

between $[POM]^{6-}$ and γ-CD using the automated Interaction Site Screening (aISS)[41] algorithm implemented in the xTB program package.[35] The lowest energy isomers obtained from molecular docking were further optimized with the r^{2}SCAN-3c DFT composite functional, which proved to be accurate for conformational problems.[42] The resulting structure (M1) is presented in Fig. 3A. It shows partial inclusion of the POM into the cavity of γ-CD, where the γ-CD molecule sits obliquely across the longitudinal belt and one of the capping surfaces of the POM. Binding occurs through the –OH groups on the secondary rim of γ-CD. We considered further isomeric structures of $[POM(\gamma\text{-CD})_1]^{6-}$ with γ-CD interacting laterally over the longitudinal belt region through its secondary (isomer M2) and primary (isomer M3) rim sites. The resulting DFT-optimized structures are shown in Fig. 3B and C, respectively. For the free energy differences, we refined the r^{2}SCAN-3c electronic energies with ωB97X-V[43]/def2-QZVPP.[50] While M1 and M2 have similar free energies, M3 has an ~1.13 eV higher free energy (0.80 eV with r^{2}SCAN-3c) (see the details in Table S2), suggesting that M3 is a less favorable form. The small energy difference between M1 and M2 does not indicate a clear preference of one structure over another and is within the error of the applied methods for such complexes. However, in the experiment, only one conformer was observed (at a resolution of ~140, FWHM of the $[POM(\gamma\text{-CD})_1]^{6-}$ peak is 4.8 Å^2, Fig. 2).

To identify which one of those two conformers is observed in the experiment, we calculated the CCS values of the DFT-optimized structures with the trajectory method (TM) in IMoS 1.9 using the optimized Lennard-Jones (LJ) parameters for W reported earlier, *i.e.* ε = 3.75 meV and σ = 4.40 Å,[51] instead of the default parameters of IMoS (ε = 2.60 meV and σ = 3.5 Å). Thereby, we considered the quadrupole interactions that are expected to be important due to the high negative charge of the complexes. With the optimized LJ parameters for W, we obtained better agreement with the experiment in the case of the parent $[HPOM]^{5-}$ (Fig. S4) for which the possible structural types are more constrained than those for the γ-CD adducts. The condensed phase structure of $[POM]^{6-}$ is known from crystallography data[14,52] and the $[HPOM]^{5-}$ structure was built by adding H to possible protonation sites. With the optimized LJ parameters for W, the $^{TM}CCS_{N_2}$ value of the lowest energy structure of $[HPOM]^{5-}$ (see Fig. S4) was 516.1 Å^2 and is in very good agreement (within ~1%) with the experiment ($^{TIMS}CCS_{N_2}$ = 515.4 Å^2). When using the default LJ parameters, the calculated CCS is ~4% smaller ($^{TM}CCS_{N_2}$ = 497.6 Å^2). The values of $^{TM}CCS_{N_2}$ were 667.2 Å^2, 659.2 Å^2 and 686.4 Å^2 for M1, M2 and M3, respectively. The standard error in the values of $^{TM}CCS_{N_2}$ was <0.4%. The structure M1 ($^{TM}CCS_{N_2}$ = 667.2 Å^2) shows the best agreement with the experiment ($^{TIMS}CCS_{N_2}$ = 665.0 ± 3.1 Å^2). Although M1 and M2 were energetically similarly probable in the gas-phase, the TIMS results suggest that only M1 exists as the dominant gas-phase isomer as the possible presence of M2 can be excluded by the high-resolution ion mobility measurements. Notably, the structure M3, which shows interactions through the primary rim sites of γ-CD, can be ruled out by both energetic and $^{TIMS}CCS_{N_2}$ means, even though such interaction motifs were observed previously in the condensed phase/solution.[14] However, such a structure is energetically less favorable in the isolated state due to a smaller number of HB interactions, compared to structures that show binding through the secondary rim sites of γ-CD. Different from the gas-phase, such structures get stabilized from the overall extended packing patterns in the condensed phases or in the solution-phase.[14] To quantify this, Table S3 in the SI presents the HBs identified in the structures M1, M2 and M3. The structures M1 and M2 exhibit the highest number of intermolecular HBs, formed between the secondary OH groups of γ-CD and the O atoms of the POM. In contrast, the structure M3—where the POM is coordinated through the primary OH rim of γ-CD—exhibits a lower number of intermolecular HBs between γ-CD and the POM and the lengths of the intramolecular HBs in the secondary rim sites of γ-CD all exceed 2 Å. Consequently, M3 exhibits a lower overall HB stabilization energy compared to M1 and M2. This line of reasoning can, in principle, also be applied to larger systems in which the POM is coordinated by multiple γ-CD units. In such cases, the spatial arrangement and nature of the OH groups involved

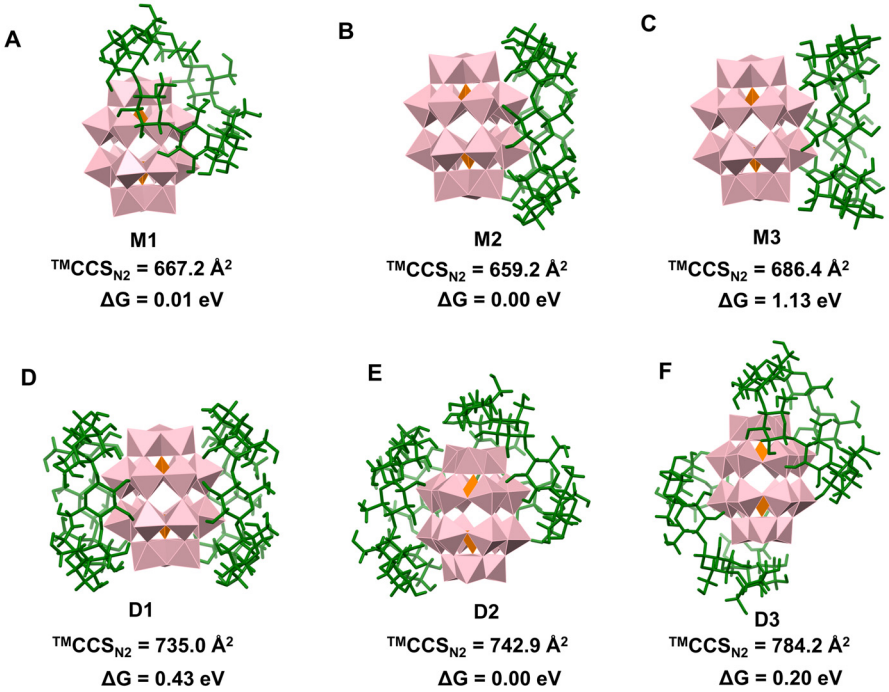

Fig. 3 DFT optimized isomeric structures of (A–C) $[POM(\gamma\text{-CD})_1]^{6-}$ and (D–F) $[POM(\gamma\text{-CD})_2]^{6-}$. Color codes: pink: WO_6 octahedron, orange: PO_4 tetrahedron, green: γ-CD. Δ*G* is the relative change in free energy in the gas-phase, computed using the ωB97X-V/def2-TZVPP method for M1–M3 (A–C) and the r^2SCAN-3c method for the larger D1–D3 (D–F). Individual energetic contributions are listed in the SI. Standard error in $^{TM}CCS_{N_2}$ values was <0.4%. (POM = $P_2W_{18}O_{62}$).

in coordination would similarly influence the HB network and stabilization energy.

3.4.2. Gas-phase structure of conformers of $[POM(\gamma\text{-CD})_2]^{6-}$. Similarly, we considered several isomeric structures of $[POM(\gamma\text{-CD})_2]^{6-}$ by varying the site of attachment of the γ-CDs on the POM surface. In isomer D1 (Fig. 3D), the two γ-CD molecules were attached on opposite sides of the longitudinal belt region (long axis) of the POM, such that the POM lies sandwiched between the two γ-CD molecules. In isomer D2 (Fig. 3E), one γ-CD interacts laterally over the longitudinal surface and the other obliquely over the longitudinal and capping surface. In isomer D3, both γ-CD molecules were placed obliquely over the POM surface (interaction site similar to M1) at opposite sides. In all cases, the interaction of the γ-CD molecules was considered through the secondary rim, which offers more HB interactions, as already observed in the case of $[POM(\gamma\text{-CD})_1]^{6-}$. Interactions through the primary rim sites will lead to energetically significantly less favorable structures and hence they are not considered further. Among the calculated structures, D1 was the most compact isomer with $^{TM}CCS_{N_2}$ of 735.0 Å^2 and could be assigned to the isomer (i) observed in the experiment ($^{TIMS}CCS_{N_2}$ of 728.6 ± 0.5 Å^2). The structure D2 ($^{TM}CCS_{N_2}$ of 742.9 Å^2) could explain the larger isomer (ii) ($^{TIMS}CCS_{N_2}$ of 738.4 ± 0.4 Å^2) observed in the experiment (Fig. 2B). The $^{TM}CCS_{N_2}$ of D3 was 784.2 Å^2, which was much larger compared to the experimentally observed ones, and hence, its possible existence could be ruled out. Regarding the free energy difference, D2 was the energetically most stable structure, followed by D1 (0.43 eV higher in energy compared to D2), further supporting the findings that D1 and D2 have $^{TIMS}CCS_{N_2}$ values that match the experiment. However, it has to be noted that the energy evaluation might be less accurate than for the $[POM(\gamma\text{-CD})_1]^{6-}$ structures as the Hessian calculations of vibration for the thermo-contributions were carried out with GFN1-xTB and the single-point Hessian approach[53] instead of r^2SCAN-3c due to the larger size and electronic complexity of the adducts. Furthermore, ωB97X-V/def2-QZVPP energy refinement of the r2SCAN-3c electronic energies was not feasible.

3.4.3. Gas-phase structure of conformers of $[POM(\gamma\text{-CD})_3]^{6-}$. For $[POM(\gamma\text{-CD})_3]^{6-}$, four distinct isomers were observed in TIMS MS studies (Fig. 2), as the additional γ-CD molecule leads to a larger number of possible stable isomers. The isomeric structures of $[POM(\gamma\text{-CD})_3]^{6-}$ (T1–T4) simulated are shown in Fig. 4 and were generated considering different patterns of packing of the three γ-CD molecules on the POM surface. Due to the larger size of the adducts, DFT geometry optimizations were not feasible and all calculations were limited to the semi-empirical GFN1-xTB level. To estimate the errors introduced by the GFN1-xTB geometry optimizations, we compared the DFT-optimized structure of M1 to the result of a GFN1-xTB optimization (Fig. S5). $^{TM}CCS_{N_2}$ of the GFN1-xTB optimized structure was smaller by 1.3% compared to that predicted by DFT as the NCI contacts were generally closer. The RMSD between the DFT and GFN1-xTB structures was 0.38 Å, suggesting that GFN1-xTB could also be used to predict the

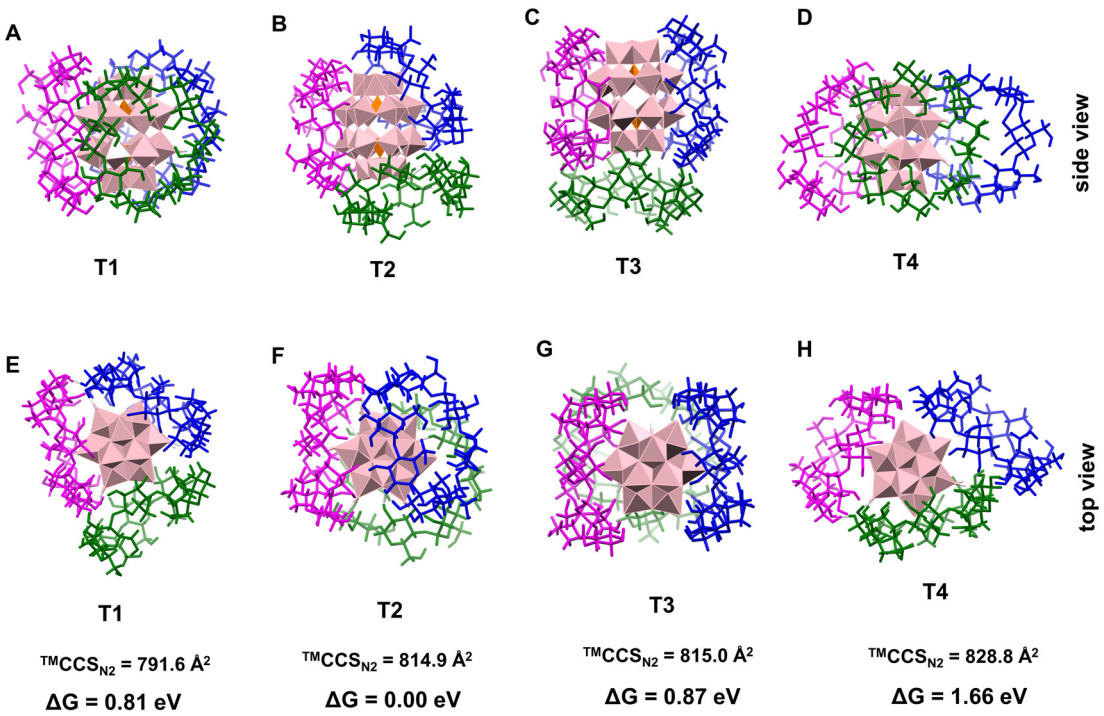

Fig. 4 GFN1-xTB optimized structures of different conformers of $[POM(\gamma\text{-CD})_3]^{6-}$. The view along the longitudinal side (long axis) is shown with A–D and along the capping surface with E–H. Color codes: pink: WO_6 octahedron, orange: PO_4 tetrahedron, three γ-CDs are colored differently in blue, green and pink, white: H transferred to the POM surface or bonded between two γ-CDs. The standard error in the mean values of $^{TM}CCS_{N_2}$ denoted here is <0.4%. The ΔG values were calculated with GFN1-xTB.

topology of the adducts qualitatively, but larger errors compared to DFT are expected. Furthermore, in structures T1–T4, proton transfer from the –OH groups of the γ-CD to the O atoms on the POM surface occurred. This is likely an artifact of GFN1-xTB as it was also observed when optimizing smaller adducts with GFN1-xTB where DFT optimizations did not show a proton transfer (Fig. S5). However, such small effects are unlikely to affect $^{TM}CCS_{N_2}$. In all these simulated structures, binding of γ-CD to the POM surface was again considered through the larger secondary rim to maximize the number of HB interactions. The view of the structures T1–T4 along the longitudinal side is presented in Fig. 4A–D and the view along the capping surface is in Fig. 4E–H, respectively. In T1 (Fig. 4A and E), three γ-CDs were packed over the longitudinal surface of the POM, leading to a compact structure with the surface around the long axis of the POM completely wrapped by the γ-CD molecules. In T2 (Fig. 4B and F), one γ-CD binds laterally over the longitudinal surface. On the opposite side of the POM relative to this γ-CD, the other two γ-CDs bind obliquely across the two capping sites. The structure T2 can be visualized to hierarchically grow from the lower adduct D2, where an additional γ-CD attaches over the exposed surface of the POM in D2. In isomer T3 (Fig. 4C and G), two γ-CDs bind on opposite sides of the longitudinal surface of the POM and the third CD binds on one of the capping surfaces. This structure T3 can also be considered to hierarchically grow from D1, with an additional γ-CD covering one of the capping surfaces of D1. In T4 (Fig. 4D and H), the three γ-CDs were arranged over the longitudinal surface of the POM, but here the γ-CDs were less compactly packed compared to isomer T1. The structures T1–T4 show $^{TM}CCS_{N_2}$ values of 791.6, 814.9, 815.0 and 828.8 Å^2, respectively. This agrees with the range of $^{TIMS}CCS_{N_2}$ values of the four isomers observed in the experiment (790.6 ± 0.6 Å^2, 798.7 ± 0.6 Å^2, 821.2 ± 0.6 Å^2 and 825.1 ± 0.5 Å^2). While the errors observed in the computations are larger due to the limited applicability of precise methods, TIMS MS and theoretical studies revealed that in isolated states, multiple isomers exist in a $[POM(\gamma\text{-CD})_3]^{6-}$ complex due to different binding patterns of the γ-CD molecules over the POM surface. A comparison between the experimental $^{TIMS}CCS_{N_2}$ values and $^{TM}CCS_{N_2}$ values for the calculated structures is given in Table 1.

3.5. Effect of counter ions (K^+) and charge state on the conformational space of the POM and γ-CD adducts

We further performed TIMS measurements on $[KPOM(\gamma\text{-CD})_1]^{5-}$. Different from $[POM(\gamma\text{-CD})_1]^{6-}$, where only one isomer was observed (Fig. 2), the TIMS spectra of $[KPOM(\gamma\text{-CD})_1]^{5-}$, presented in Fig. 5A, clearly show two distinct isomers with $^{TIMS}CCS_{N_2}$ values of 593.9 ± 0.6 Å^2 and 605.2 ± 1.0 Å^2. This revealed the role of the counter ions in controlling the conformer-space of these adducts, as upon attachment of the K^+ ion, more isomeric structures are stable.

Table 1 Comparison of $^{TIMS}CCS_{N_2}$ (mean values) of the observed species and $^{TM}CCS_{N_2}$ of the calculated structures that matched best with the experiment

Species	$^{TIMS}CCS_{N_2}$ (Å^2)	$^{TM}CCS_{N_2}$ (Å^2)
$[POM(\gamma\text{-CD})_1]^{6-}$	665.0 (i)	667.2 (M1)
$[POM(\gamma\text{-CD})_2]^{6-}$	728.6 (i)	735.0 (D1)
	738.4 (ii)	742.9 (D2)
$[POM(\gamma\text{-CD})_3]^{6-}$	790.6 (i)	791.6 (T1)
	798.7 (ii)	814.9 (T2)
	821.2 (iii)	815.0 (T3)
	825.1 (iv)	828.8 (T4)
$[KPOM(\gamma\text{-CD})_1]^{5-}$	593.9 (i)	597.3 (M′1)
	605.2 (ii)	609.7 (M′2)

Similar to $[POM(\gamma\text{-CD})_1]^{5-}$, several possible structures of the isomeric $[KPOM(\gamma\text{-CD})_1]^{5-}$ were optimized with r^{2}SCAN-3c and refined with ωB97X-V/def2-QZVPP electronic energies. The lowest energy structures with matching $^{TM}CCS_{N_2}$ values are presented in Fig. 5B and C. Isomer M′1 shows binding of γ-CD laterally over the longitudinal surface of the POM and the K^+ ion on the opposite surface. Isomer M′2 shows binding of the γ-CD obliquely over one of the capping surfaces and the longitudinal surface with K^+ on an adjacent site on the longitudinal surface. The $^{TM}CCS_{N_2}$ of M′1 is 597.3 Å^2, which matches the experimentally observed isomer (i) ($^{TIMS}CCS_{N_2}$ of 593.9 Å^2). The isomer M′2 with a $^{TM}CCS_{N_2}$ value of 609.7 Å^2 corresponds to isomer (ii) ($^{TIMS}CCS_{N2}$ of 605.2 Å^2) in the experiment. The other isomeric structures which were considered with K^+ attached over the capping surface are shown in Fig. S6. A structure with γ-CD attached laterally over the longitudinal surface like M′1 but with K^+ over the capping surface (Fig. S6A) showed a $^{TM}CCS_{N_2}$ value of 600.3 Å^2 and hence its possible existence in the experiment cannot be ruled out by CCS alone. However, its free energy was higher by 0.67 eV compared to M′2 and is unlikely to be present in the experiment. A structure similar to M′2 but with the K^+ position over the capping surface (opposite to the side of γ-CD) could also be ruled out due to its 0.54 eV higher free energy than that of M′2, and a $^{TM}CCS_{N_2}$ value of 619.0 Å^2 (Fig. S6B), which is much higher compared to the experimentally observed values.

We further performed TIMS measurements for $[KPOM(\gamma\text{-CD})_n]^{5-}$ (n = 2, 3) and $[K_2POM(\gamma\text{-CD})_n]^{4-}$ (n = 1–3). The spectra and $^{TIMS}CCS_{N_2}$ values are presented in Fig. S7 and Table S1. Similarly to the previously discussed result, they revealed that for a fixed number of γ-CD molecules attached to the POM, the conformer stability is strongly affected by the number of K^+ ions attached and hence the overall charge state of the species.

3.6. CID studies on $[POM(\gamma\text{-CD})_n]^{6-}$ (n = 1–3) complexes

In order to further probe the nature of the interaction between the POM and the γ-CD, we performed collisional excitation of the $[POM(\gamma\text{-CD})_n]^{6-}$ (n = 1–3) complexes with N_2. Transfer of protons from γ-CD to the POM surface was observed during the detachment of γ-CD from the POM surface. The proton transfer to the POM surface was also followed by the loss of water molecules, suggesting that decomposition of the POM can occur inside the γ-CD cavity (Fig. S8–S10). This is consistent with the fragmentation behavior of CD complexes of Keggin and Lindqvist POMs, which has been observed earlier.[54]

3.7. Anion PES studies on POMs and their adducts with γ-CD

3.7.1. PES experiments to determine experimental electron binding energies (EBEs). To investigate how non-covalent complexation of CDs with POMs affects their electronic structures, we performed anion PES on the multicharged POM anions and their respective γ-CD adducts. A previously reported machine[40] (PES coupled to an IMS MS platform) was used for the PES measurements. Note that the ion mobility resolution of the IMS cell in this setup is ~30 and hence the isomers observed on the high resolution TIMS platform (as described above) were not resolvable here. All the isomers of a particular species contribute to the PES spectra that will be discussed below. Note that in principle two different ESI sources operating under different conditions may not make the same isomer

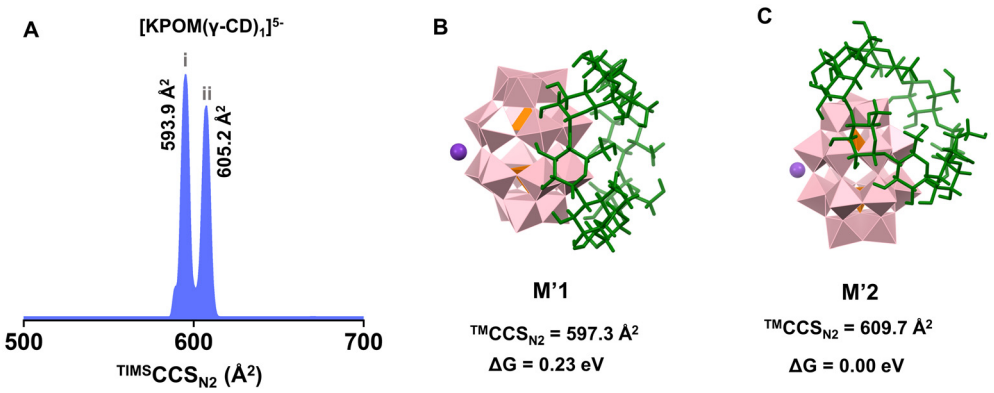

Fig. 5 (A) TIMS spectra of $[KPOM(\gamma\text{-CD})_1]^{5-}$, (B and C) DFT-optimized lowest energy structures of $[KPOM(\gamma\text{-CD})_1]^{5-}$. $^{TIMS}CCS_{N_2}$ values denote the mean values over three measurements. The standard error is ≤1.0 Å^2. ΔG is the relative free energy, computed using the ωB97X-V/def2-TZVPP method. Color codes: pink: WO_6 octahedron, orange: PO_4 tetrahedron, green: γ-CD.

distribution. However, given the host–guest nature of the adducts generated, we expect identical overall structure types and assume that identical isomer distributions are generated.

The PES spectrum of the parent $[KPOM]^{5-}$ anion was measured at a detachment wavelength of 210 nm. This clearly showed the presence of two bands (Fig. 6A). PES spectra of $[KPOM]^{5-}$ were recorded at higher wavelengths of 220 nm and 240 nm (Fig. S11). The spectra allowed us to estimate the corresponding ADE (adiabatic detachment energy), VDE (vertical detachment energy) and RCB (repulsive Coulomb barrier). For $[KPOM]^{5-}$, the corresponding ADE was determined to be −2.6 ± 0.5 eV (reflecting the threshold on the lower electron binding energy (EBE) side) and VDE was assigned as −1.3 ± 0.4 eV to reflect the maximum of the first band. The negative values of the EBEs indicate that the $[KPOM]^{5-}$ anion is electronically metastable in the gas-phase, but the repulsive Coulomb barrier (RCB) prevents significant electron tunneling autodetachment before UV laser irradiation. Autodetachment of an electron from the $[HPOM]^{5-}$ electronic ground state was also observed using an Orbitrap instrument, which showed e-detachment half-lives of 40–100 s (depending on experimental conditions), when the parent ion was isolated in the ion trap (Fig. S12). From the PES experiment, the RCB was determined to be 4.0 ± 0.3 eV (from the spectral cutoff at the higher EBE – see also discussion in the SI). Negative EBEs have also been previously reported for similar POMs such as $PVW_{11}O_{40}^{4-}$ (ADE: −0.90 eV and VDE: −0.63 eV).[55] In contrast, Keggin type anions such as $[PM_{12}O_{40}]^{3-}$ were highly stable in the gas-phase with an ADE of 1.7 eV for M = Mo and 2.1 eV for M = W, respectively.[56]

Similarly, PES spectra were also recorded for the adduct $[KPOM(\gamma\text{-CD})_1]^{5-}$ at 210 nm (Fig. 6B) and the measured ADEs were used to determine the stabilization of the $[KPOM]^{5-}$ anion resulting from complexation with γ-CD. For $[KPOM(\gamma\text{-CD})_1]^{5-}$, the ADE was determined to be −0.2 ± 0.3 eV (Fig. 6B). The ADE value showed a significant shift to a higher EBE for $[KPOM(\gamma\text{-CD})_1]^{5-}$ compared to that of $[KPOM]^{5-}$, suggesting that binding of the $[KPOM]^{5-}$ anion in the cavity of γ-CD stabilizes the anion electronically by ∼2.4 eV. We further performed PES measurements on the adducts $[POM(\gamma\text{-CD})_1]^{6-}$ (Fig. 6C) and $[POM(\gamma\text{-CD})_2]^{6-}$ (Fig. 6D) at 210 nm and the ADEs of these anions were −2.0 ± 0.5 eV and −1.4 ± 0.4 eV, respectively. Here also, complexation of a second γ-CD molecule to $[POM(\gamma\text{-CD})_1]^{6-}$ stabilizes the anion and increases the ADE by ∼0.6 eV. The isolated POM (without γ-CD complexation) was not observed in the 6^- charge state in the gas-phase, so comparison with the $[POM]^{6-}$ anion could not be made to assess the stabilization by the addition of the first γ-CD molecule. Experimental errors are higher for faster electrons due to the unavailability of suitable calibration systems in the negative EBE side. For the adducts with γ-CD, PES spectra could not be obtained at longer wavelengths and hence their VDE and RCB were not determined. PES measurements could not be performed on other γ-CD adducts of the POM due to poor signal intensity in the PES setup.

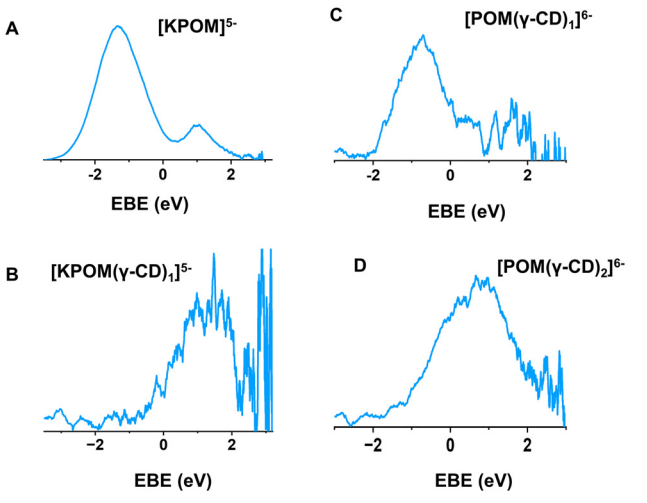

Fig. 6 Negative ion photoelectron spectroscopy (PES) spectra of (A) $[KPOM]^{5-}$, (B) $[KPOM(\gamma\text{-CD})_1]^{5-}$, (C) $[POM(\gamma\text{-CD})_1]^{6-}$ and (D) $[POM(\gamma\text{-CD})_2]^{6-}$, measured at 210 nm. EBE denotes the electron binding energy.

3.7.2. Calculated ADEs and discussion on electron binding energies (EBEs). The theoretical ADEs of $[KPOM]^{5-}$ were predicted with PBE0[57]-D4[58]/def2-QZVPP to be −1.74 eV, while the range-separated hybrid ωB97X-V/def2-QZVPP yielded −1.19 eV. While these rather large deviations between both hybrid methods already indicate larger errors predicting ADEs for such electronically complex systems, the overall trend of negative EBEs supports the experimental observation as discussed below. For the larger $[KPOM(\gamma\text{-CD})_1]^{5-}$, no converged wavefunction could be achieved with PBE0, so only the ωB97X-V/def2-QZVPP result was considered further. Here, the calculated ADE for $[KPOM(\gamma\text{-CD})_1]^{5-}$ was determined to be +1.68 eV. This is again a large shift compared to the experiment (−0.2 ± 0.3 eV), but it is ∼2.9 eV higher than the predicted value for $[KPOM]^{5-}$ and agrees well with the trend in the experiment (∼2.4 eV increase of the ADE upon CD complexation). Hence, this confirms the electronic stabilization of the $[KPOM]^{5-}$ anion upon complexation with neutral γ-CD, which can also be deduced from a Born–Haber cycle, as shown in Fig. S13. According to Fig. S13, the electronic stabilization due to complexation with γ-CD can be expressed as

$$\begin{aligned}\Delta\mathrm{ADE} &= \mathrm{ADE}([\mathrm{KPOM}]^{5-}) - \mathrm{ADE}([\mathrm{KPOM}(\gamma\text{-CD})]^{5-}) \\ &= \Delta\Delta G_b([\mathrm{KPOM}(\gamma\text{-CD})]^{4-}) \\ &\quad - \Delta\Delta G_b([\mathrm{KPOM}(\gamma\text{-CD})]^{5-})\end{aligned} \quad (1)$$

where $\mathrm{ADE}([KPOM]^{5-})$ and $\mathrm{ADE}([KPOM(\gamma\text{-CD})]^{5-})$ are the adiabatic electron detachment energies of $[KPOM]^{5-}$ and $[KPOM(\gamma\text{-CD})]^{5-}$ and $\Delta\Delta G_b$ ($[KPOM(\gamma\text{-CD})]^{4-}$) and $\Delta\Delta G_b$ ($[KPOM(\gamma\text{-CD})]^{5-}$) are the binding free energies of γ-CD to the POM anions. Such approaches have also been used earlier to estimate BEs from PES data for other systems.[59,60] The binding free energies were calculated with ωB97X-V/def2-QZVPP elec-

tronic energies and GFN1-xTB thermo corrections *via* a single-point Hessian approach for the r^{2}SCAN-3c optimized structures. The $\Delta\Delta G_b$ values for γ-CD binding to $[KPOM]^{5-}$ and $[KPOM]^{4-}$ were −6.5 eV and −3.8 eV, respectively. The stabilization of $[KPOM]^{5-}$ by complexation with γ-CD can be estimated from the binding energy difference of ∼2.7 eV (ΔADE = −3.8 − (−6.5 eV) = 2.7 eV) in reasonable agreement with the experiment (∼2.4 eV). A similar phenomenon was also observed in the case of negative ion PES measurements on boron clusters, where the inclusion of $B_{12}X_{12}^{2-}$ clusters in the cavity of CDs resulted in an increase in their electronic stability.[11] Moreover, PES studies on such non-covalent complexes of $B_{12}X_{12}^{2-}$ clusters with CDs revealed the existence of two distinct RCBs arising from electron detachment from $B_{12}X_{12}^{2-}$ and ionization of the neutral CD molecule.[61]

4. Conclusion

In summary, we report a joint experimental and theoretical investigation on the geometrical and electronic structures of the non-covalent adducts of γ-CD with a POM in their isolated states. Using TIMS studies, we demonstrate that supramolecular adducts of γ-CD with the POM show distinct conformers in their isolated states (gas-phase) in contrast to their condensed phase structures, which show one dominant form. The gas-phase topologies are also different compared to their previously reported solution-phase or condensed-phase forms.[14] Moreover, attachment of counter ions and charge states of the adducts also affected the nature of the conformer formation in the gas-phase. The geometrical structures were resolved through comparison of experimentally observed $^{TIMS}CCS_{N_2}$ with $^{TM}CCS_{N_2}$, *i.e.* calculated CCS of computationally predicted structures. Moreover, anion PES studies revealed that the EBE (ADE) of the POM anion significantly increases upon complexation with γ-CD, suggesting that electronic stabilization of the POM anion occurs upon complexation with the γ-CD cavity. Our work provides significant insights into the geometrical and electronic structures of non-covalent complexes of the POM and γ-CD, which will enable better designing of supramolecular hybrids in the future. Moreover, the observation of different structures in the gas-phase compared to the structures formed in the solution phase or condensed-phase suggests that new types of supramolecular assemblies can be created by preparative MS methods,[62,63] which cannot be accessed by conventional condensed phase routes. Deposition of *m*/*z*-selected ions on surfaces by the method of ion soft-landing has been used in the past to create novel materials (most recently even alternating between mass-selected ions and mass-selected counterions).[62] A future direction would be to couple IM techniques to such ion-deposition systems to allow isomer-selective deposition of *m*/*z*-selected ions. Mass and isomer-selected $[POM(\gamma\text{-CD})_n]$ complexes could be deposited on different surfaces or ionic liquids to create new materials with properties related to their gas-phase assembly.

Author contributions

P. C. and M. M. K. conceived the project. P. C. performed the ESI MS and TIMS MS studies. M. L. performed the PES studies. C. P. performed the DFT and xTB calculations under the supervision of S. G. M. N. also performed some of the xTB calculations and the IMoS calculations. P. W. performed the autodetachment studies using Orbitrap. M. I. synthesized the POM. The manuscript was written through contributions of all the authors.

Conflicts of interest

There are no conflicts of interest to declare.

Data availability

The data supporting the findings of this study are included in the SI. Raw data underlying the results of this article are available in the RADAR4Chem repository at **https://doi.org/10.22000/vc5ya7kvqb87bq60**.

Supplementary information contains additional details on materials and methods used, additional ESI MS and CID data, PES data, additional computational data and co-ordinates of optimized calculated structures. See DOI: **https://doi.org/10.1039/d5nr02831k**.

Acknowledgements

C. P. thanks Merck KGaA for financial support. M. I., P. C., M. N. and M. M. K. acknowledge support from the Helmholtz Association through the Research Program Materials Systems Engineering (MSE) within the Programme-Oriented Funding scheme (POF IV) at Karlsruhe Institute of Technology (KIT). M. I., P. W., M. L. and M. M. K. also acknowledge support from the Deutsche Forschungsgemeinschaft (DFG, German Research Foundation) through the Collaborative Research Centre "4f for Future" (CRC 1573, projects A2, B4, C1 and C3). P. C. thanks Alexander von Humboldt Foundation for her postdoctoral research fellowship during initial stages of the work.

References

1 M. C. T. Fyfe and J. F. Stoddart, *Acc. Chem. Res.*, 1997, **30**, 393–401.
2 S. Datta, M. L. Saha and P. J. Stang, *Acc. Chem. Res.*, 2018, **51**, 2047–2063.
3 H. Zhu, L. Chen, B. Sun, M. Wang, H. Li, J. F. Stoddart and F. Huang, *Nat. Rev. Chem.*, 2023, **7**, 768–782.
4 X. Ma and Y. Zhao, *Chem. Rev.*, 2015, **115**, 7794–7839.
5 J. Szejtli, *Chem. Rev.*, 1998, **98**, 1743–1754.

6 K. Uekama, F. Hirayama and T. Irie, *Chem. Rev.*, 1998, **98**, 2045–2076.
7 T. Irie and K. Uekama, *Adv. Drug Delivery Rev.*, 1999, **36**, 101–123.
8 A. Nag, P. Chakraborty, A. Thacharon, G. Paramasivam, B. Mondal, M. Bodiuzzaman and T. Pradeep, *J. Phys. Chem. C*, 2020, **124**, 22298–22303.
9 A. Mathew, G. Natarajan, L. Lehtovaara, H. Häkkinen, R. M. Kumar, V. Subramanian, A. Jaleel and T. Pradeep, *ACS Nano*, 2014, **8**, 139–152.
10 D. Prochowicz, A. Kornowicz and J. Lewiński, *Chem. Rev.*, 2017, **117**, 13461–13501.
11 Z. Li, Y. Jiang, Q. Yuan, J. Warneke, Z. Hu, Y. Yang, H. Sun, Z. Sun and X.-B. Wang, *Phys. Chem. Chem. Phys.*, 2020, **22**, 7193–7200.
12 K. I. Assaf, M. S. Ural, F. Pan, T. Georgiev, S. Simova, K. Rissanen, D. Gabel and W. M. Nau, *Angew. Chem., Int. Ed.*, 2015, **54**, 6852–6856.
13 A. Nag, P. Chakraborty, G. Paramasivam, M. Bodiuzzaman, G. Natarajan and T. Pradeep, *J. Am. Chem. Soc.*, 2018, **140**, 13590–13593.
14 M. A. Moussawi, N. Leclerc-Laronze, S. Floquet, P. A. Abramov, M. N. Sokolov, S. Cordier, A. Ponchel, E. Monflier, H. Bricout, D. Landy, M. Haouas, J. Marrot and E. Cadot, *J. Am. Chem. Soc.*, 2017, **139**, 12793–12803.
15 Y. Wu, R. Shi, Y.-L. Wu, J. M. Holcroft, Z. Liu, M. Frasconi, M. R. Wasielewski, H. Li and J. F. Stoddart, *J. Am. Chem. Soc.*, 2015, **137**, 4111–4118.
16 P. Yang, W. Zhao, A. Shkurenko, Y. Belmabkhout, M. Eddaoudi, X. Dong, H. N. Alshareef and N. M. Khashab, *J. Am. Chem. Soc.*, 2019, **141**, 1847–1851.
17 S. Yao, C. Falaise, S. Khlifi, N. Leclerc, M. Haouas, D. Landy and E. Cadot, *Inorg. Chem.*, 2021, **60**, 7433–7441.
18 L. Ni, H. Li, H. Xu, C. Shen, R. Liu, J. Xie, F. Zhang, C. Chen, H. Zhao, T. Zuo and G. Diao, *ACS Appl. Mater. Interfaces*, 2019, **11**, 38708–38718.
19 P. Su, X. Zhu, S. M. Wilson, Y. Feng, H. Y. Samayoa-Oviedo, C. Sonnendecker, A. J. Smith, W. Zimmermann and J. Laskin, *Chem. Sci.*, 2024, **15**, 11825–11836.
20 N. I. Gumerova and A. Rompel, *Nat. Rev. Chem.*, 2018, **2**, 0112.
21 D. Wang, L. Liu, J. Jiang, L. Chen and J. Zhao, *Nanoscale*, 2020, **12**, 5705–5718.
22 M. R. Horn, A. Singh, S. Alomari, S. Goberna-Ferrón, R. Benages-Vilau, N. Chodankar, N. Motta, K. Ostrikov, J. MacLeod, P. Sonar, P. Gomez-Romero and D. Dubal, *Energy Environ. Sci.*, 2021, **14**, 1652–1700.
23 S. Zhu, H. Pang, Z. Sun, S. U. Khan, G. Mustafa, H. Ma, X. Wang and G. Yang, *Dalton Trans.*, 2024, **53**, 13248–13279.
24 T. Ma, R. Yan, X. Wu, M. Wang, B. Yin, S. Li, C. Cheng and A. Thomas, *Adv. Mater.*, 2024, **36**, 2310283.
25 W. Wang, X. Wang, J. Cao, J. Liu, B. Qi, X. Zhou, S. Zhang, D. Gabel, W. M. Nau, K. I. Assaf and H. Zhang, *Chem. Commun.*, 2018, **54**, 2098–2101.
26 C. Falaise, M. A. Moussawi, S. Floquet, P. A. Abramov, M. N. Sokolov, M. Haouas and E. Cadot, *J. Am. Chem. Soc.*, 2018, **140**, 11198–11201.
27 S. Khlifi, S. Yao, C. Falaise, P. Bauduin, V. Guérineau, N. Leclerc, M. Haouas, H. Salmi-Mani, P. Roger and E. Cadot, *Chem. – Eur. J.*, 2024, **30**, e202303815.
28 B. T. Ruotolo, J. L. P. Benesch, A. M. Sandercock, S.-J. Hyung and C. V. Robinson, *Nat. Protoc.*, 2008, **3**, 1139–1152.
29 E. Kalenius, M. Groessl and K. Rissanen, *Nat. Rev. Chem.*, 2019, **3**, 4–14.
30 M. Göth and K. Pagel, *Anal. Bioanal. Chem.*, 2017, **409**, 4305–4310.
31 C. Bleiholder and M. T. Bowers, *Annu. Rev. Anal. Chem.*, 2017, **10**, 365–386.
32 S. Daly, A. Kulesza, F. Poussigue, A.-L. Simon, C. M. Choi, G. Knight, F. Chirot, L. MacAleese, R. Antoine and P. Dugourd, *Chem. Sci.*, 2015, **6**, 5040–5047.
33 A. J. Surman, P. J. Robbins, J. Ujma, Q. Zheng, P. E. Barran and L. Cronin, *J. Am. Chem. Soc.*, 2016, **138**, 3824–3830.
34 P. J. Robbins, A. J. Surman, J. Thiel, D.-L. Long and L. Cronin, *Chem. Commun.*, 2013, **49**, 1909–1911.
35 C. Bannwarth, E. Caldeweyher, S. Ehlert, A. Hansen, P. Pracht, J. Seibert, S. Spicher and S. Grimme, *Wiley Interdiscip. Rev.: Comput. Mol. Sci.*, 2021, **11**, e1493.
36 S. Grimme, C. Bannwarth and P. Shushkov, *J. Chem. Theory Comput.*, 2017, **13**, 1989–2009.
37 C. Drummond, L. Pérez-Fuentes and D. Bastos-González, *J. Phys. Chem. C*, 2019, **123**, 28744–28752.
38 C. R. Graham and R. G. Finke, *Inorg. Chem.*, 2008, **47**, 3679–3686.
39 S. M. Stow, T. J. Causon, X. Zheng, R. T. Kurulugama, T. Mairinger, J. C. May, E. E. Rennie, E. S. Baker, R. D. Smith, J. A. McLean, S. Hann and J. C. Fjeldsted, *Anal. Chem.*, 2017, **89**, 9048–9055.
40 M. Vonderach, O. T. Ehrler, P. Weis and M. M. Kappes, *Anal. Chem.*, 2011, **83**, 1108–1115.
41 C. Plett and S. Grimme, *Angew. Chem., Int. Ed.*, 2023, **62**, e202214477.
42 S. Grimme, A. Hansen, S. Ehlert and J.-M. Mewes, *J. Chem. Phys.*, 2021, **154**, 064103.
43 N. Mardirossian and M. Head-Gordon, *Phys. Chem. Chem. Phys.*, 2014, **16**, 9904–9924.
44 F. Neese, F. Wennmohs, U. Becker and C. Riplinger, *J. Chem. Phys.*, 2020, **152**, 224108.
45 C. Larriba-Andaluz and C. J. Hogan Jr, *J. Chem. Phys.*, 2014, **141**, 194107.
46 H. Kim, H. I. Kim, P. V. Johnson, L. W. Beegle, J. L. Beauchamp, W. A. Goddard and I. Kanik, *Anal. Chem.*, 2008, **80**, 1928–1936.
47 M. E. Ridgeway, M. Lubeck, J. Jordens, M. Mann and M. A. Park, *Int. J. Mass Spectrom.*, 2018, **425**, 22–35.
48 P. Chakraborty, M. Neumaier, P. Weis and M. M. Kappes, *J. Am. Soc. Mass Spectrom.*, 2023, **34**, 676–684.
49 C. Przybylski and V. Bonnet, *Carbohydr. Polym.*, 2022, **297**, 120019.

50 F. Weigend and R. Ahlrichs, *Phys. Chem. Chem. Phys.*, 2005, **7**, 3297–3305.
51 S. Hupin, V. Tognetti, F. Rosu, S. Renaudineau, A. Proust, G. Izzet, V. Gabelica, C. Afonso and H. Lavanant, *Phys. Chem. Chem. Phys.*, 2022, **24**, 16156–16166.
52 B. Dawson, *Acta Crystallogr.*, 1953, **6**, 113–126.
53 S. Spicher and S. Grimme, *J. Chem. Theory Comput.*, 2021, **17**, 1701–1714.
54 P. Su, A. J. Smith, J. Warneke and J. Laskin, *J. Am. Soc. Mass Spectrom.*, 2019, **30**, 1934–1945.
55 O. M. Primera-Pedrozo, S. Tan, D. Zhang, B. T. O'Callahan, W. Cao, E. T. Baxter, X.-B. Wang, P. Z. El-Khoury, V. Prabhakaran, V.-A. Glezakou and G. E. Johnson, *Nanoscale*, 2023, **15**, 5786–5797.
56 T. Waters, X. Huang, X.-B. Wang, H.-K. Woo, R. A. J. O'Hair, A. G. Wedd and L.-S. Wang, *J. Phys. Chem. A*, 2006, **110**, 10737–10741.
57 C. Adamo and V. Barone, *J. Chem. Phys.*, 1999, **110**, 6158–6170.
58 E. Caldeweyher, S. Ehlert, A. Hansen, H. Neugebauer, S. Spicher, C. Bannwarth and S. Grimme, *J. Chem. Phys.*, 2019, **150**, 154122.
59 X.-B. Wang, *J. Phys. Chem. A*, 2017, **121**, 1389–1401.
60 M. B. Knickelbein and W. J. C. Menezes, *J. Chem. Phys.*, 1991, **94**, 4111–4119.
61 Y. Jiang, Z. Hu, Y. Yang, P. Peng, C. Zhong, H. Sun, Z. Sun and X.-B. Wang, *J. Phys. Chem. Lett.*, 2023, **14**, 6736–6742.
62 P. Su, H. Hu, J. Warneke, M. E. Belov, G. A. Anderson and J. Laskin, *Anal. Chem.*, 2019, **91**, 5904–5912.
63 F. Yang, M. Moors, D. A. Hoang, S. Schmitz, M. Rohdenburg, H. Knorke, A. Charvat, X.-B. Wang, K. Y. Monakhov and J. Warneke, *ACS Appl. Nano Mater.*, 2022, **5**, 14216–14220.